RSC Advances

ROYAL SOCIETY OF CHEMISTRY

PAPER

View Article Online
View Journal | View Issue

Cite this: *RSC Adv.*, 2026, **16**, 2685

Dopant-driven electronic coupling and fast gas sensing in gold-boron co-doped Si/MoS$_2$ heterostructures: a first-principles study

Trong Nhan Duong,[abc] Nguyen Vo Anh Duy,[d] Nguyen Thanh Son,[e] Chi Minh Phan,[f] Duy Khanh Nguyen[ab] and Minh Triet Dang*[c]

Received 28th October 2025
Accepted 29th December 2025

DOI: 10.1039/d5ra08262e

rsc.li/rsc-advances

Developing gas sensors that combine ultrahigh sensitivity, chemical selectivity, and rapid recovery is crucial for next-generation environmental and industrial monitoring technologies. Here, density functional theory is employed to unravel the structural, electronic, and interfacial mechanisms governing CO and CO$_2$ detection on pristine, single-doped, and AuB co-doped silicene/MoS$_2$ heterostructures. Phonon and formation-energy analyses confirm that AuB co-doping markedly enhances thermodynamic and dynamic stability while inducing a semiconductor-to-metal transition through hybridized Au d, B p, and Si p states near the Fermi level. The resulting metallic character enables efficient carrier delocalization and rapid electronic response. Adsorption, charge-density-difference, and periodic energy decomposition analyses reveal distinct interaction pathways: CO adsorption arises primarily from orbital hybridization between Au d and C p orbitals, whereas CO$_2$ binding is dominated by electrostatic attraction and B p–O p coupling. Balanced electrostatic and orbital components, together with moderate Pauli repulsion, ensure strong yet reversible adsorption, promoting fast charge transfer without surface trapping. The AuB co-doped interface achieves the highest performance, exhibiting charge transfer up to 0.0104*e* and recovery times as short as 0.050 ns, surpassing most reported two-dimensional sensors. These ultimate effects of Au-induced polarization and B-mediated electron acceptance establish a tunable electronic platform that simultaneously enhances sensitivity, selectivity, and reusability. This work provides atomistic insight into dopant-controlled interfacial chemistry and charts a rational pathway for designing multifunctional 2D heterostructure sensors with rapid, reliable, and energy-efficient gas detection.

1. Introduction

The escalating need for precise air quality monitoring has intensified research into advanced gas sensors. Modern devices must combine high sensitivity and selectivity with rapid response and stability to effectively safeguard public health and industrial safety.[1–4] Two-dimensional (2D) materials, such as graphene, transition-metal dichalcogenides (TMDs), and MXenes, have emerged as promising candidates for gas sensing,[5–13] due to their high surface-to-volume ratio and tunable electronic properties.[14–17] In particular, their ability to operate at room temperature with high sensitivity makes them suitable for next-generation sensing platforms.

Molybdenum disulfide (MoS$_2$) is widely studied among TMDs for gas-sensing applications owing to its intrinsic semiconducting properties, high carrier mobility, and strong adsorption capabilities.[18,19] Specifically, monolayer MoS$_2$ exhibits a direct band gap of approximately 1.8 eV, advantageous for modulating its electronic behavior upon interaction with gas molecules.[20,21] Nevertheless, pristine MoS$_2$ faces inherent limitations, including slow and often incomplete recovery attributed to the layered structure of stacked S–Mo–S sheets, which restricts efficient molecular gas interactions.[18] On the other hand, silicene, a silicon-based analog of graphene, has attracted considerable interest for its distinctive buckled honeycomb lattice and graphene-like electronic properties.[22,23] Unlike the perfectly planar graphene, silicene's buckled architecture, comprising two silicon sublattices positioned at varying heights, induces unique electronic and spintronic functionalities.[23] The integration of MoS$_2$ and silicene into a heterostructure is a promising strategy for enhancing gas-sensing performance by leveraging the synergistic electronic

---

[a] Laboratory for Computational Physics, Institute for Computational Science and Artificial Intelligence, Van Lang University, Ho Chi Minh City, Vietnam. E-mail: nhan.duongtrong@vlu.edu.vn
[b] Faculty of Mechanical, Electrical, and Computer Engineering, Van Lang School of Technology, Van Lang University, Ho Chi Minh City, Vietnam
[c] Can Tho University, 3-2 Road, Can Tho, Vietnam. E-mail: dmtriet@ctu.edu.vn
[d] FPT University, Can Tho Campus, 600 Nguyen Van Cu Street, Ninh Kieu, Can Tho, Vietnam
[e] Lac Hong University, 10 Huynh Van Nghe Street, Dong Nai Province, Vietnam
[f] Chemical Engineering Discipline, WASM: MECE, Curtin University, Perth, Australia

properties and surface interaction mechanisms of both materials.[24] Nonetheless, pristine forms of MoS_2 and silicene continue to face challenges in selectivity and sensitivity to specific gases, thereby restricting their widespread practical deployment. To surmount these limitations, constructing van der Waals (vdW) heterostructures and employing chemical functionalization *via* targeted doping are being explored as viable avenues to refine electronic properties and augment the sensing capabilities of 2D materials. Van der Waals heterostructures, in particular, exhibit superior gas-sensing potential due to pronounced charge-transfer phenomena and structural stability attributed to vdW bonding, surpassing that of covalently bonded counterparts. Furthermore, their ability to regenerate effectively upon desorption of gas molecules significantly enhances their practical utility.[18,25–27]

In this study, a silicene/MoS_2 (Si/MoS_2) heterostructure is proposed as a promising platform for developing high-performance gas sensors. To enhance its sensing capability, the heterostructure is modified through dual doping with gold (Au) and boron (B) for the detection of CO and CO_2 molecules. Gold doping exploits the unique catalytic properties of Au, which enhance gas adsorption and promote efficient charge transfer between the sensing surface and target molecules. Meanwhile, boron doping tunes the electronic structure by introducing acceptor states, thereby improving the material's sensitivity and responsiveness. The simultaneous incorporation of Au and B combines these complementary effects, balancing charge distribution and enhancing both stability and selectivity. Detailed simulations of CO and CO_2 adsorption processes reveal the atomic-scale interaction mechanisms, providing essential insights into the relationship between doping, electronic modulation, and sensing performance. These findings establish a theoretical framework for designing next-generation two-dimensional material-based gas sensors with superior sensitivity and fast recovery characteristics.

2. Computational details

In this study, all geometry optimizations were performed utilizing the advanced machine-learning-based M3GNet-UP-2022 functional, as implemented in the Amsterdam Modeling Suite (AMS).[28] The M3GNet-UP-2022 potential set, trained using deep learning algorithms, offers accuracy comparable to that of the generalized gradient approximation (GGA) with the Perdew–Burke–Ernzerhof (PBE) exchange-correlation functional.[29,30]

To evaluate the thermodynamic stability of doped systems, we calculate formation energies (E_{form}), defined as:[31]

$$E_{\text{form}} = E_{\text{doped}} - E_{\text{pristine}} - \sum_i n_i \mu_i \tag{1}$$

where E_{doped} and E_{pristine} are the total energies of the doped and pristine systems, respectively; n_i denotes the number of dopant atoms added or removed; and μ_i is the chemical potential of species i.

Adsorption energies (E_{ads}) of gas molecules (*e.g.*, CO, CO_2) on the optimized substrates were determined using:[32]

$$E_{\text{ads}} = E_{\text{substrate+gas}} - E_{\text{substrate}} - E_{\text{gas}} \tag{2}$$

where $E_{\text{substrate+gas}}$, $E_{\text{substrate}}$, and E_{gas} represent the total energies of the substrate-adsorbate system, the substrate alone, and the isolated gas molecule, respectively.

Electronic properties calculations were conducted using the Vienna *Ab initio* Simulation Package (VASP),[33] employing a plane-wave basis set with a cutoff energy of 520 eV to achieve converged wavefunction expansions. The self-consistent field iterations were considered converged when the total energy difference dropped below 10^{-5} eV, and structural optimizations concluded when residual forces were less than 10^{-2} eV Å^{-1}. Brillouin zone sampling utilized an 8 × 8 × 1 Monkhorst–Pack *k*-point mesh for these two-dimensional periodic systems.[34] Exchange-correlation interactions were treated using the PBE functional within the GGA framework.[35,36] To accurately account for long-range dispersion interactions in the heterostructure and gas adsorption processes, the DFT-D3 correction was applied in all electronic property calculations.[37] For completeness, a comparison of adsorption energies with alternative van der Waals dispersion schemes (DFT-D2 and Tkatchenko–Scheffler)[38,39] is provided in the SI.

3. Results and discussion

3.1. Thermal stability of pristine and AuB co-doped silicene/MoS_2 heterostructure

To understand the structural stability and robustness of the silicene/MoS_2 heterostructure, we perform a geometric optimization using the M3GNet-UP-2022 potential set. Fig. 1 illustrates the optimized Si/MoS_2 heterostructure, showing a well-ordered arrangement where the silicene layer exhibits its characteristic buckled structure on top of the MoS_2 layer. This distinctive buckling, approximately 0.44 Å in height, arises from the weak sp^3 hybridization among silicon atoms, which is typical and starkly contrasts with the planar structure observed in graphene.[40,41] In the pristine system (Fig. 1a), the interlayer spacing (h = 3.545 Å) indicates typical van der Waals interactions, consistent with prior experimental observations for analogous two-dimensional heterostructures.[40]

To analyze the influence of doping on the structural stability, Table 1 presents detailed structural parameters and corresponding formation energies for each configuration. The results indicate that all investigated configurations display negative formation energies, signifying substantial thermodynamic stability, with E_{form} values ranging from −0.526 to −0.537 eV. Specifically, Au doping (Fig. 1b) significantly reduces the interlayer spacing to h = 2.242 Å, indicating an enhanced interaction between the silicene and MoS_2 layers facilitated by the Au atoms. This improved interaction likely arises from the formation of weak covalent bonds between Au atoms and adjacent Si and S atoms, consistent with the adsorption mechanisms reported for silicene on various metal substrates.[40,42] Conversely, boron doping configuration (Fig. 1c) only slightly reduces the interlayer distance to h = 3.185 Å while maintaining the highest formation energy of E_{form} = −0.537 eV. The cause of this difference is the small atomic radius of B (0.87

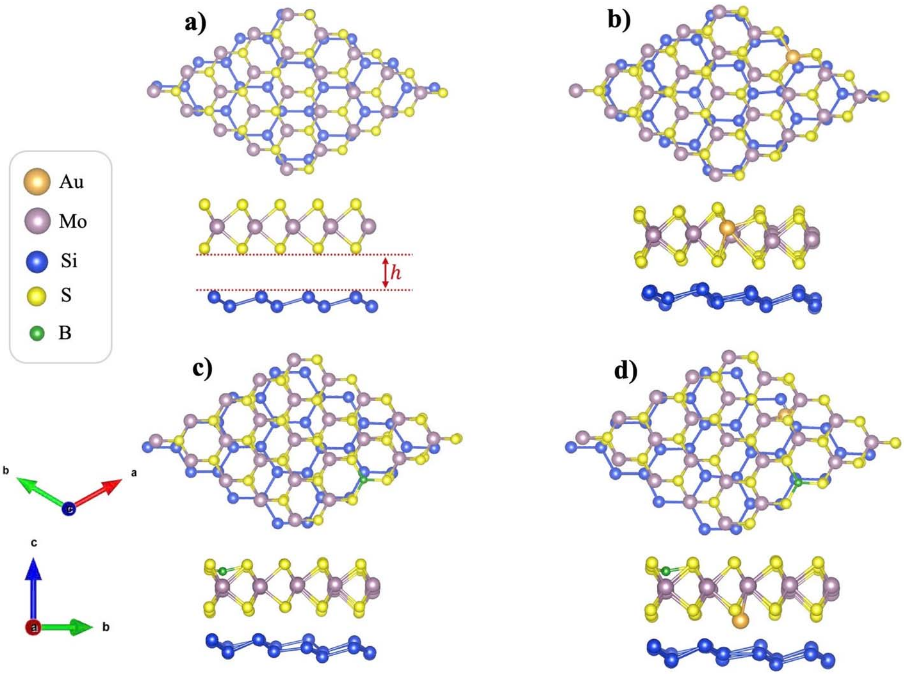

Fig. 1 Optimized geometric structures of (a) pristine Si/MoS$_2$, (b) Au-doped Si/MoS$_2$, (c) B-doped Si/MoS$_2$, and (d) AuB co-doped Si/MoS$_2$ configurations. Silicon, molybdenum, sulfur, boron, and gold atoms are marked in blue, purple, yellow, green, and orange, respectively. These configurations are obtained by the M3GNet-UP-2022 potential implemented in the SCM package.

Å) and its high electronegativity (2.04), which give rise to different electronic interactions compared to Au. Based on the two stable single-doped systems, Au-doped and B-doped silicene/MoS$_2$, co-doping was achieved by introducing the complementary heteroatom: boron into the Au-doped system and gold into the B-doped system, forming an AuB co-doped configuration. The structural stability of all models was assessed using formation energy calculations and phonon-spectrum analyses. Configurations exhibiting the lowest formation energies and no imaginary frequencies in their phonon spectra were identified as thermodynamically and dynamically stable, and thus selected as substrates for subsequent gas adsorption studies.

In the case of Au and B co-doping (Fig. 1d), the interlayer distance reaches its minimum value of h = 2.174 Å, demonstrating a synergistic effect between the two dopant elements in enhancing interlayer bonding, consistent with previously published theories on structural phase transitions in heterostructures.[43]

For the silicene layer, the Si–Si bond length increases from 2.380 Å in the pristine structure to 2.484 Å (Au-doped), 2.462 Å (B-doped), and 2.463 Å (AuB co-doped). This increase can be explained by the charge-transfer effect from the dopant atoms, which weakens the covalent Si–Si bonds.[44,45] The characteristic buckling structure of silicene, with a buckling height of approximately 0.7–0.8 Å, is affected by the doping process,

Table 1 Structural properties and formation energies of pristine and doped Si/MoS$_2$ heterostructures. These values are calculated by the M3GNet-UP-2022 potential implemented in the SCM package

Configuations/characteristics	Si/MoS$_2$	Si/MoS$_2$ Au doping	Si/MoS$_2$ B doping	Si/MoS$_2$ Au and B co-doping
E_{form} (eV)	−0.535	−0.528	−0.537	−0.526
h (Å)	3.545	2.242	3.185	2.174
Si–Si (Å)	2.380	2.484	2.462	2.463
Mo–S (Å)	2.420	2.614	2.536	2.537
S–Au (Å)	—	2.397	—	—
S–B (Å)	—	—	1.855	1.853
Mo–Au (Å)	—	—	—	2.862
Si–Si–Si (°)	112.60	119.37	118.75	118.71
S–Mo–S-1st (°)	135.70	140.73	138.11	138.10
S–Mo–S-2nd (°)	82.13	96.25	86.62	86.76
Mo–S–Mo (°)	81.82	85.78	84.63	86.37
Mo–S–Au (°)	—	100.39	—	—
Mo–S–B (°)	—	—	109.67	109.97

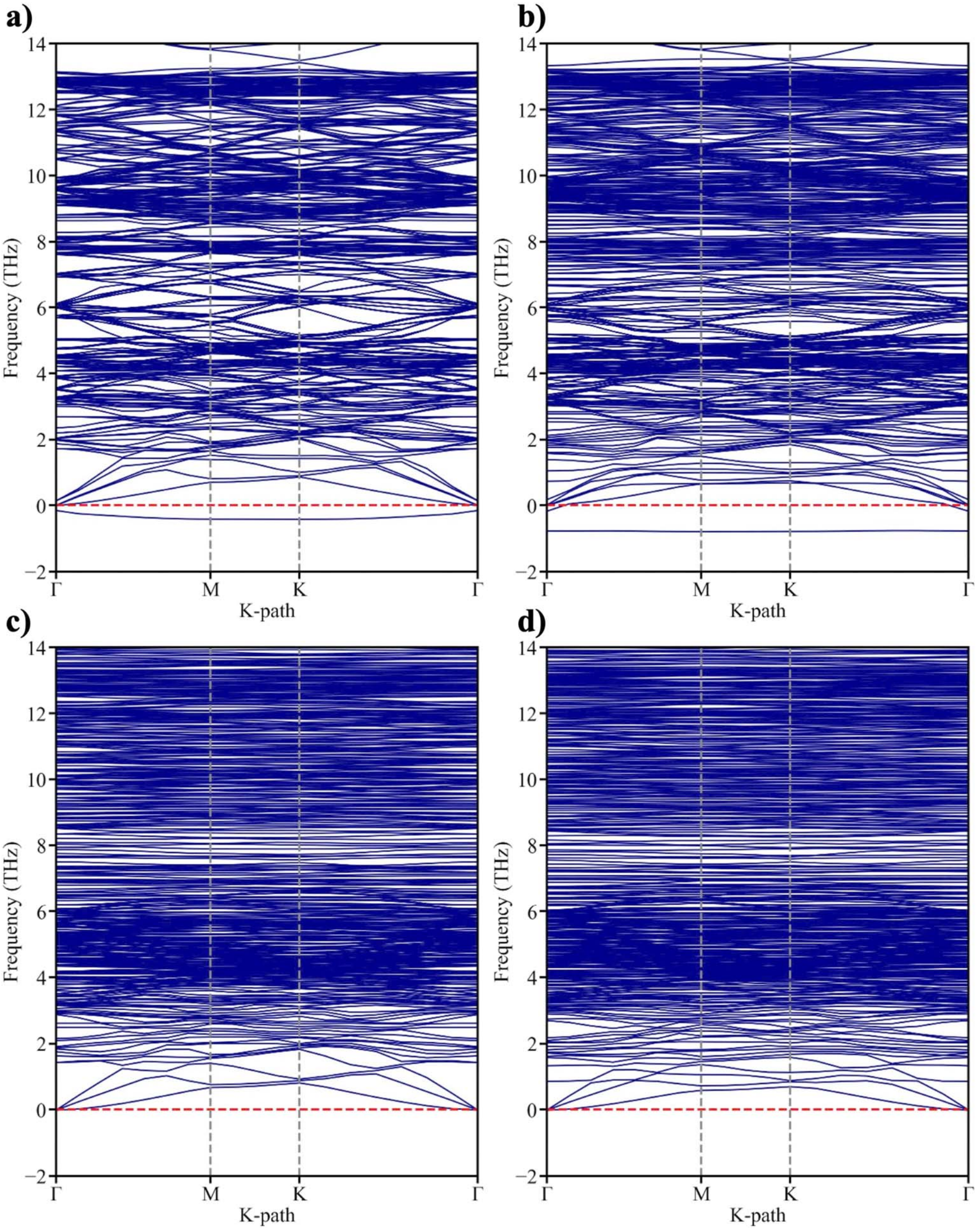

Fig. 2 Phonon spectrum of (a) pristine silicene/MoS_2, (b) silicene/MoS_2 doped Au, (c) silicene/MoS_2 doped B, and (d) silicene/MoS_2 co-doped Au and B configurations. These spectra are calculated by the M3GNet-UP-2022 potential implemented in the SCM package.

similar to reports in studies of strained silicene.[46,47] In the MoS_2 layer, the Mo–S bonds also exhibit significant variations. The Mo–S bond length increases from 2.420 Å in the pristine structure to 2.614 Å (Au-doped), 2.536 Å (B-doped), and 2.537 Å (AuB co-doped). This change reflects the influence of doping on the electronic structure and bonding properties of transition-metal dichalcogenides.[48,49] The newly formed bonds between the dopant atoms and their neighboring atoms exhibit characteristic bond lengths reflecting distinct chemical natures. The S–Au bond measures 2.397 Å, whereas the S–B bond is significantly shorter at 1.855 Å. This disparity indicates that the S–B bond possesses stronger covalent character compared to the metal–nonmetal interaction of Au–S.[50,51] In the co-doped configuration, the Mo–Au bond length is 2.862 Å, establishing a complex bonding network that influences the overall electronic properties of the system.

The Si–Si–Si bond angle increases from 112.60° in the pristine structure to 119.37° (Au-doped), 118.75° (B-doped), and 118.71° (AuB co-doped), approaching the 120° ideal of a flat configuration.[46,52] This change indicates that the silicene layer becomes flatter upon doping, reducing its characteristic buckling height.[53] This phenomenon can be explained by electronic stabilization arising from interactions with the dopant atoms and the underlying MoS_2 layer.[54] In the MoS_2 layer, bond angles exhibit complex variations. The largest S–Mo–S angle (S–Mo–S-1st) increases from 135.70° to 140.73° under Au doping, but shows only a slight increase to 138.11° with B and Au–B doping. Conversely, the smallest S–Mo–S angle (S–Mo–S-2nd) and Mo–

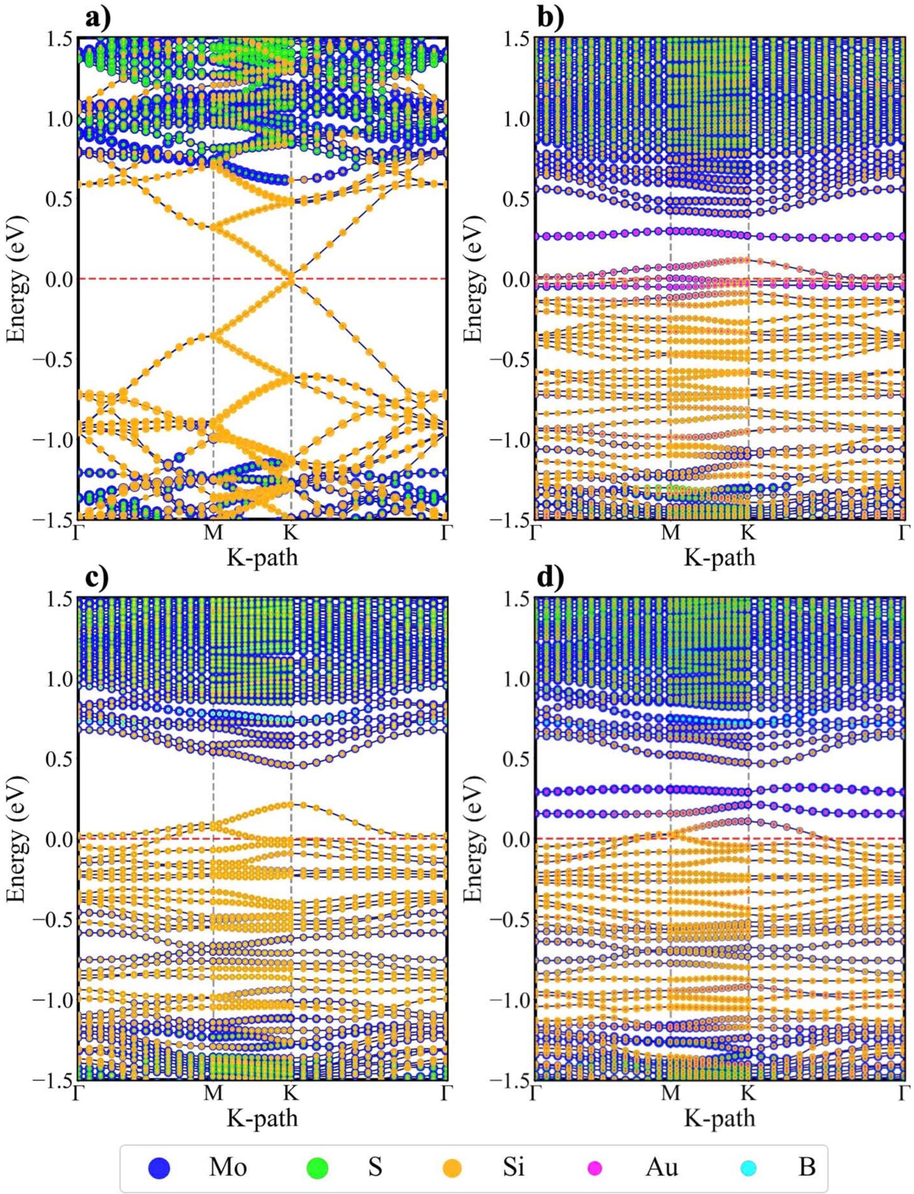

Fig. 3 Electronic band structures of (a) pristine silicene/MoS_2, (b) Au-doped silicene/MoS_2, (c) B-doped silicene/MoS_2, and (d) AuB co-doped silicene/MoS_2 configurations. The Fermi level indicated by the red dashed lines is set to zero. These band structures are calculated by the DFT-D3 potential implemented in the VASP package.

S–Mo angle demonstrate an increasing trend across all doped configurations, rising from 82.13° and 81.82° to approximately 85–96° depending on the dopant type. This distortion reflects localized structural deformation in TMDCs upon dopant incorporation[55] The newly formed Mo–S–Au (100.39°) and Mo–S–B (109.67°) bond angles reveal differences in bonding mechanisms and chemical environments around dopant atoms. The larger Mo–S–B angle indicates stronger repulsion due to boron's small atomic size, leading to greater local distortion in the MoS_2 lattice and potentially significantly affecting electronic properties and the material's applicability in gas-sensing devices.

To evaluate the thermodynamic stability of the doped systems, we calculate the phonon spectra of all investigated configurations in Fig. 2. The absence of imaginary parts of phonon frequencies across the entire Brillouin zone confirms complete dynamic stability. For the pristine and Au-doped systems, the phonon spectra reveal acoustic modes in the low-frequency region (below 2 THz) and optical modes in the high-frequency region (2–14 THz). Particularly significant is the out-of-plane acoustic (ZA) mode in silicene, which exhibits low energy due to weak sp^2 hybridization. This has been experimentally confirmed as the primary cause of reduced electron mobility in silicene compared to graphene.[56] The ZA phonon mode plays a decisive role in charge-transport properties and can be strongly influenced by substrate interactions, as demonstrated in studies of room-temperature silicene transistors.[40]

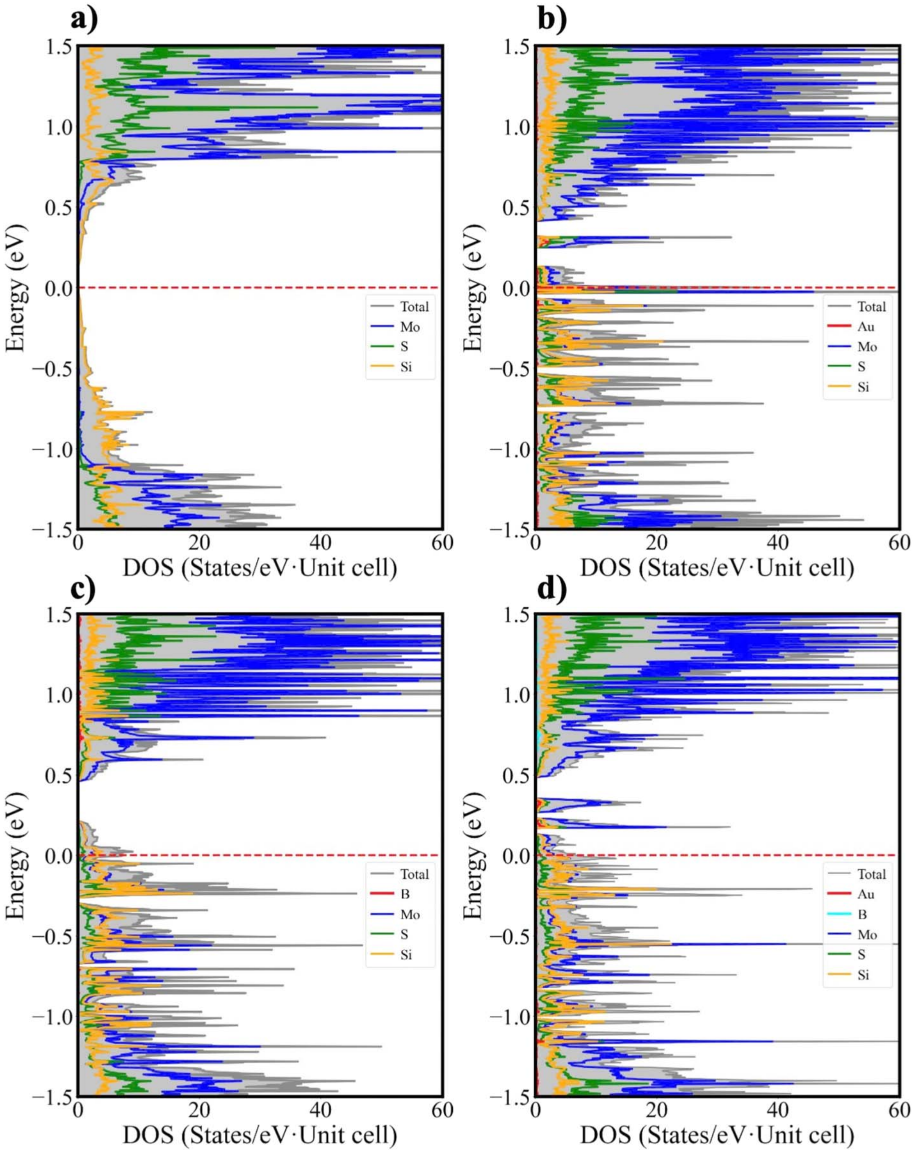

Fig. 4 Projected density of states (pDOS) of (a) pristine silicene/MoS_2, (b) Au-doped silicene/MoS_2, (c) B-doped silicene/MoS_2, and (d) AuB co-doped silicene/MoS_2 configurations. The Fermi level indicated by the dashed red lines is set to zero. These pDOS are calculated by the DFT-D3 potential implemented in the VASP package.

Detailed analysis indicates that B-doped and AuB co-doped systems exhibit substantially higher phonon mode density, reflecting increased lattice complexity due to dopant incorporation. This modification to the phonon spectrum may affect the material's thermal and mechanical properties, as observed in molecular dynamics simulations of Si/MoS_2 heterostructures.[57] These results provide a critical theoretical foundation for designing and optimizing tunable gas sensors based on Si/MoS_2 heterostructures through selective doping.

3.2. Electronic properties of pristine and AuB co-doped silicene/MoS_2 heterostructure

To further investigate the electronic properties of the supported material systems, the band structure and density of states were analyzed. As shown in Fig. 3a, the pristine silicene/MoS_2 heterostructure exhibits semiconducting behavior with a band gap of approximately 0.05 eV, indicating its near-metallic character. This small gap arises from a slight breaking of the sublattice symmetry in silicene due to weak interaction with the MoS_2 substrate, in stark contrast to gapless free-standing silicene.[58] The band structure further reveals partial preservation of silicene's characteristic Dirac cone at the *K* point, albeit with mild distortion induced by van der Waals coupling to MoS_2.

The incorporation of Au dopants induces a complete transition of the electronic character from semiconducting to metallic, as shown in Fig. 3b. Au atoms introduce states within the original band gap, eliminating the gap and yielding metallic behavior. The projected density of states (pDOS) analysis in Fig. 4b reveals a substantial contribution from Au d orbitals in the energy region near the Fermi level, leading to strong hybridization with the S p orbitals of MoS_2 and the Si p orbitals

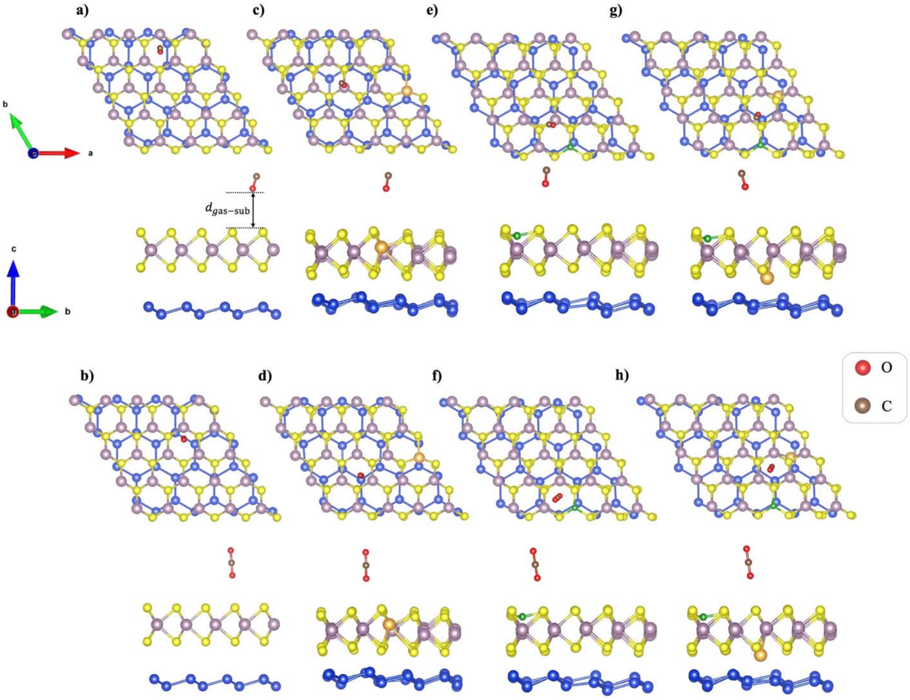

Fig. 5 The optimized structures of CO and CO_2 adsorbed on pristine silicene/MoS_2 (a and b), silicene/MoS_2 doped Au (c and d), silicene/MoS_2 doped B (e and f), and silicene/MoS_2 co-doped Au and B (g and h). These configurations are obtained by the DFT-D3 potential implemented in the VASP package.

of silicene. This effect arises from Au's metallic nature and its ability to donate electrons to the system, thereby increasing the density of states at the Fermi level and enabling metallic conductivity. Similarly, in Fig. 4c, B p orbitals contribute significantly to the conduction band, resulting in a continuous density of states at the Fermi level. The metallic character in the B-doped system is attributed to the formation of gap states due to boron's small atomic radius (0.87 Å) and its strong interaction with the host lattice, leading to an overlap of energy bands. In the case of AuB co-doping (Fig. 3d), the system likewise exhibits metallic behavior with a high, continuous density of states at the Fermi level. The analysis in Fig. 4d reveals a complex interplay between the Au d and B p orbitals, resulting in a metallic band structure with numerous hybridized states near the Fermi level. The synergistic effect of Au and B not only enhances structural stability but also delivers superior metallic conductivity compared to systems doped with Au or B individually.

3.3. Gas adsorption on pristine and doped silicene/MoS_2

3.3.1. The optimized geometric structures of the adsorption systems. To reliably identify the most stable adsorption geometries, the adsorption analysis was carried out in two successive steps. In the first step, an extensive configurational screening was performed using the M3GNet-UP-2022 machine-learning potential. All eight possible adsorption configurations for each gas-substrate system were considered, including four high-symmetry adsorption sites (top, bridge, hollow, and valley) and two representative molecular orientations (vertical and parallel), as illustrated in Fig. S2. This screening step enabled an efficient exploration of the large configurational space, and the resulting adsorption energies for all configurations are summarized in Table S3 (see SI).

In the second step, the most energetically favorable adsorption geometries identified by the M3GNet-based screening were selected for refined DFT calculations using the PBE functional as implemented in VASP, with explicit inclusion of van der Waals corrections (see Table S4). The adsorption configurations shown in Fig. 5 correspond to the global minimum-energy states obtained from DFT-D3 calculations in VASP. All remaining configurations exhibited significantly higher adsorption energies and were therefore excluded from further electronic-structure analysis to maintain clarity and focus on the physically relevant adsorption mechanisms.

Analysis of the optimized structures in Fig. 5 reveals that the CO molecule adopts a consistent adsorption configuration across all investigated systems, with the oxygen atom oriented toward the substrate surface. This orientation is observed in all four material systems: pristine (Fig. 5a), B-doped (Fig. 5c), Au-doped (Fig. 5e), and AuB co-doped (Fig. 5g) silicene/MoS_2. Such orientation can be rationalized by the electronic properties of the CO molecule, in which the oxygen atom, with a higher electronegativity (3.44) than carbon (2.55), preferentially interacts with positively charged regions on the surface. The adsorption distance $d_{\text{gas-sub}}$ of CO shows a systematic decrease upon doping: the pristine system exhibits the most significant separation (3.914 Å), followed by the Au-doped system (3.810 Å), the B-doped system (3.652 Å), and the shortest distance in the

Table 2 Comparison of adsorption parameters for CO and CO_2 gas on pristine and doped silicene/MoS_2. These values are calculated by the DFT-D3 potential implemented in the VASP package

		Substrate			
Gases	Characteristics	Silicene/MoS_2 pristine	Silicene/MoS_2 Au-doped	Silicene/MoS_2 B-doped	Silicene/MoS_2 AuB co-doped
CO	$d_{\text{gas-sub}}$ (Å)	3.914	3.810	3.652	3.518
	E_{ads} (meV)	−72.3	−70.6	−73.7	−71.2
	Recovery time (ns)	0.016	0.015	0.017	0.016
	Charge transfer (e)	0.0044	0.0045	0.0048	0.0051
CO_2	$d_{\text{gas-sub}}$ (Å)	3.051	2.970	2.754	2.520
	E_{ads} (meV)	−111.9	−120.5	−124.5	−101.1
	Recovery time (ns)	0.076	0.106	0.124	0.050
	Charge transfer (e)	0.0101	0.0101	0.0102	0.0104

AuB co-doped system (3.518 Å). This trend aligns with a previous report on gas adsorption behavior of MoS_2, demonstrating that dopant incorporation can substantially enhance gas-surface interactions.[59]

The CO_2 gas exhibits a more complex adsorption configuration while retaining its characteristic linear geometry. As illustrated in Fig. 5b, d, f and h, CO_2 preserves its straight-line structure with the oxygen atoms oriented toward the substrate surface. The adsorption distance of CO_2 is significantly shorter than that of CO in all studied systems, ranging from 3.051 Å (pristine) to 2.520 Å (co-doped). This variation reflects CO_2's larger dipole moment and stronger van der Waals interactions, in agreement with previous DFT investigations of gas adsorption on MoS_2.[60] Changes in adsorption distances upon doping can be attributed to alterations in the electronic density of states and the surface charge distribution. Boron doping, characterized by a small atomic radius (0.87 Å) and electron-deficient nature, induces pronounced modifications in the electronic structure, resulting in a substantial decrease in adsorption distance. Although Au doping exerts a more negligible effect compared to B, it still generates a notable reduction in adsorption distance due to Au's metallic character and high polarizability. Crucially, the AuB co-doped system exhibits a marked synergistic effect, achieving the shortest adsorption distance, which reflects an optimal combination of Au's metallic properties and B's electron-acceptor behavior.

3.3.2. The adsorption energies and charge transfers. Table 2 reveals a marked difference in adsorption energies between CO and CO_2 on silicene/MoS_2 systems. For the pristine system, CO exhibits an adsorption energy of −72.3 meV, whereas CO_2 reaches −111.9 meV, corresponding to an interaction strength that is approximately 23% greater than that of CO. This disparity arises from CO_2's linear molecular structure with two highly electronegative oxygen atoms, which endows it with a larger dipole moment and multiple potential interaction sites on the material surface compared to the simpler CO molecule.[61] This trend persists uniformly across all doped systems examined. The B-doped system shows the strongest adsorption, with CO at −73.7 meV and CO_2 at −124.5 meV representing increases of 2% and 11%, respectively, relative to the pristine system. This enhancement is consistent with boron's electron-deficient character, which generates Lewis acid active sites that interact effectively with gas molecules possessing lone-pair electrons, such as CO and CO_2.[62]

The incorporation of Au dopants exhibits a distinct effect, with a slight reduction in adsorption energies compared to the pristine system (CO: −70.6 meV; CO_2: −120.5 meV). Although Au is a noble metal capable of interacting with CO *via* back-donation, within this bilayer configuration, it may induce charge redistribution that diminishes the surface activity of silicene. Conversely, the AuB co-doped system demonstrates an intriguing synergistic effect, achieving a CO_2 adsorption energy of −101.1 meV, indicating that the combined presence of these two dopants can balance and optimize the adsorption properties. The stronger adsorption of CO_2 on the AuB co-doped Si/MoS_2 surface can be understood from the cooperative interplay of electronic-structure alignment and electrostatic interactions. From an orbital perspective, CO adsorption is dominated by conventional σ-donation and π-back-donation interactions with the Au site, which provide only moderate stabilization. In contrast, CO_2 adsorption is significantly enhanced by the presence of B-derived localized states near the Fermi level, which exhibit favorable energetic alignment with the low-lying LUMO ($2\pi_u$) of the CO_2 molecule. This orbital overlap facilitates charge redistribution and promotes the activation of the otherwise chemically inert CO_2 molecule. In addition to this orbital effect, electrostatic interactions play a decisive role: the B dopant acts as a Lewis-acidic center, generating a localized region of positive electrostatic potential that strongly attracts the electron-rich oxygen atoms of CO_2, which possesses a pronounced quadrupole moment. Such electrostatic attraction is substantially weaker for the nonpolar CO molecule. The combined contribution of efficient orbital coupling and enhanced electrostatic stabilization, therefore, results in a markedly stronger and more selective adsorption of CO_2 compared with CO, consistent with the DFT-D3 adsorption energies observed for the AuB co-doped system.

Analysis of the Bader charge transfer (Table 2) reveals a clear trend consistent with the adsorption energetics. CO_2 induces substantially larger charge transfer than CO across all systems, with values of 0.0101–0.0104*e* for CO_2 compared to 0.0044–0.0051*e* for CO, reflecting its stronger electron-accepting character arising from the presence of two electronegative O atoms and low-lying π* orbitals. Among all configurations, the AuB co-doped structure exhibits the highest charge transfer for both gases (CO: 0.0051 e; CO_2: 0.0104 e), indicating that the interplay between electron-deficient B sites and metallic Au atoms establishes an efficient charge-transfer pathway. This enhanced interfacial charge redistribution is a key factor underlying the superior sensing performance, consistent with experimental reports by Pham *et al.*, demonstrating that strong charge transfer can enable gas detection down to the ppb (parts-per-billion) limit.[63] Although the charge transfer per adsorbed molecule ($\sim 0.01e$) is modest at the single-molecule level, its cumulative impact under realistic sensing conditions is non-negligible. Assuming a moderate surface coverage of $\theta = 1\%$, representative of ppm-ppb gas exposure on a standard 2D channel (atomic density $n_{atom} \approx 10^{15}\ cm^{-2}$),[64] the induced carrier density change (Δn) can be estimated using the equation $\Delta n \approx \theta \times n_{atom} \times \Delta q$, the induced carrier density variation in a two-dimensional MoS_2 channel is estimated to be on the order of $10^{11}\ cm^{-2}$, comparable to the intrinsic carrier density of pristine MoS_2. This level of carrier modulation corresponds to a 10–100% change in carrier concentration and, owing to the linear dependence of conductivity on carrier density, results in a pronounced change in channel conductivity. Such resistance variations are well within the detection limits of conventional electrical readout circuits. They are consistent with previous experimental studies reporting robust sensing responses for similar charge-transfer magnitudes in 2D materials.[20,65] Therefore, the calculated charge transfer of 0.0104e associated with CO_2 adsorption, particularly in the AuB co-doped system, is sufficient to induce a measurable and reliable electrical signal, confirming the practical detectability of the proposed sensing mechanism.

The recovery time (τ) is the critical parameter for evaluating gas-sensor performance. It represents the time required for complete desorption of gas molecules from the material surface and is calculated as[7] $\tau = \upsilon^{-1}\exp\left(-\frac{E_{ads}}{k_BT}\right)$, where υ, k_B, and T denote the attempt frequency ($10^{12}\ s^{-1}$),[66] Boltzmann constant, and temperature, respectively. The calculated recovery times at 300 K for CO and CO_2 on pristine and doped silicene/MoS_2 are summarized in Table 2. CO exhibits markedly faster recovery, ranging from 0.015 ns to 0.017 ns, whereas CO_2 ranges from 0.050 ns to 0.124 ns. This inverse relationship between recovery time and adsorption energy is consistent with the Arrhenius desorption model. Gold doping exhibits a marked enhancement in CO recovery time (0.015 ns, ~6% faster than the pristine system). In comparison, the AuB co-doped configuration

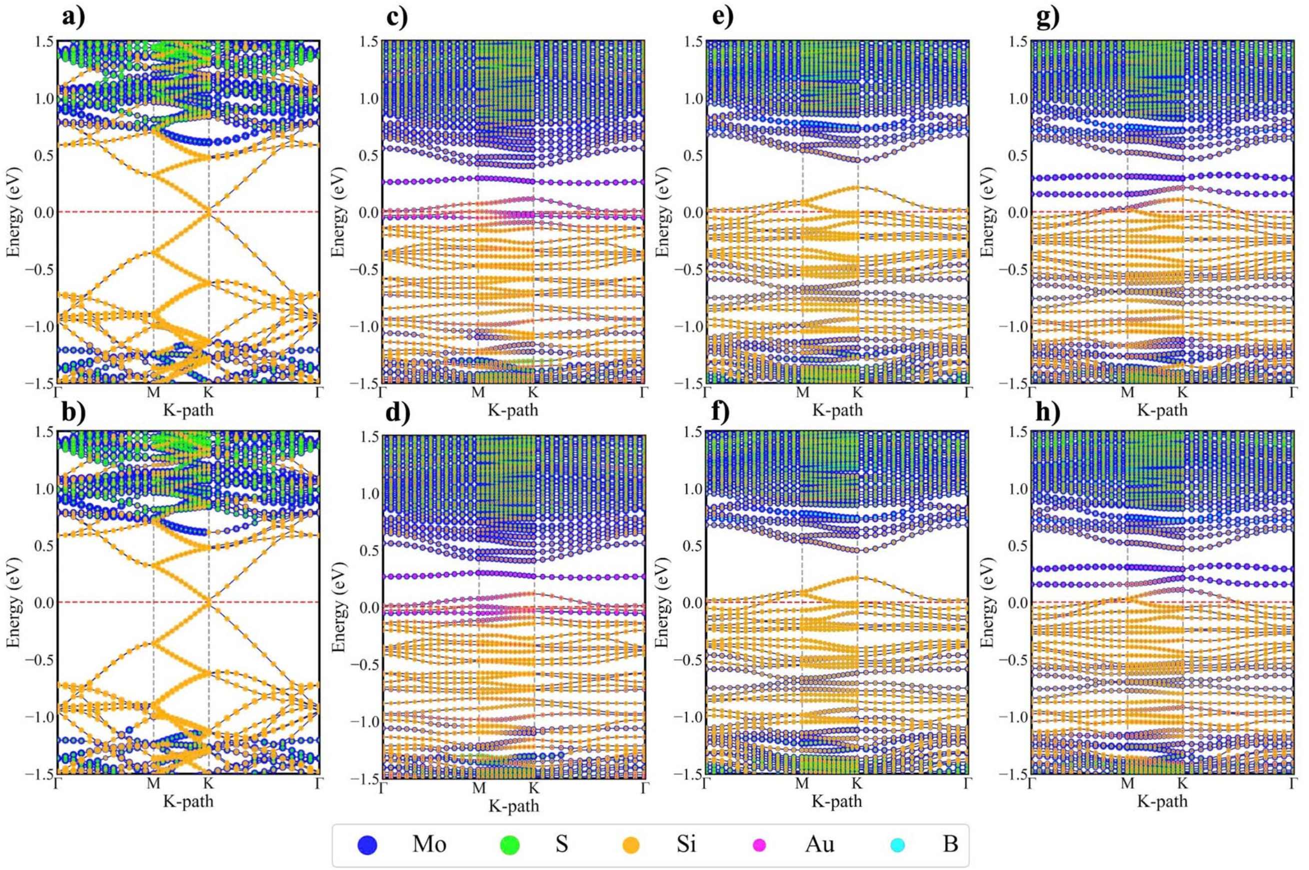

Fig. 6 Electronic band structure of CO and CO_2 adsorbed on pristine (a and b), Au-doped (c and d), B-doped (e and f), and AuB co-doped silicene/MoS_2 (g and h), respectively. The red-dashed line indicates the Fermi level. These band structures are calculated by the DFT-D3 potential implemented in the VASP package.

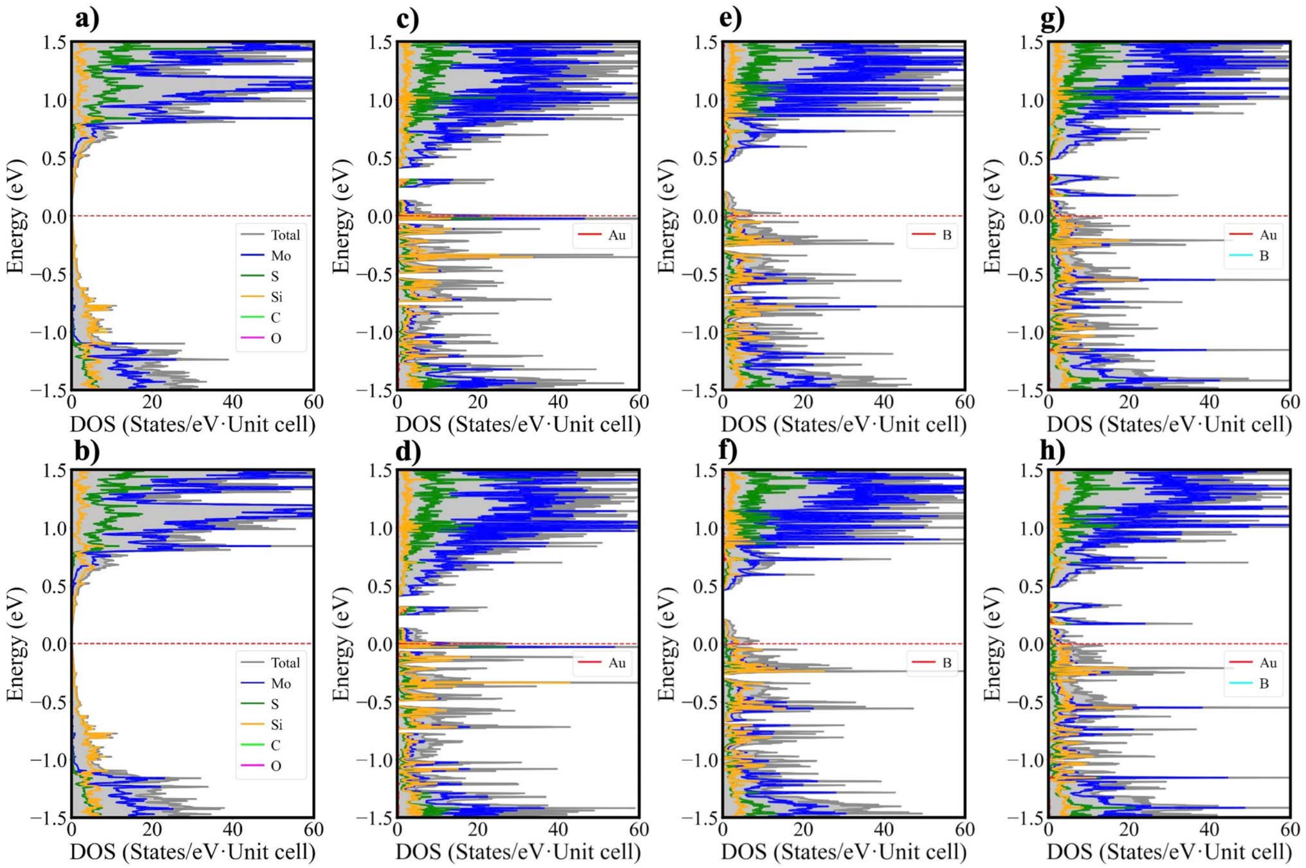

Fig. 7 Project density of states of CO and CO_2 adsorbed on pristine (a and b), Au-doped (c and d), B-doped (e and f), and AuB co-doped Si/MoS_2 co-doped Si/MoS_2 (g and h), respectively. The dashed line demonstrates the Fermi level. These pDOS are calculated by the DFT-D3 potential implemented in the VASP package.

achieves optimal performance for CO_2 with 0.050 ns, approximately 34% faster than the pristine system (0.076 ns). This improvement can be attributed to the synergistic effect of co-dopants which balances strong adsorption with rapid desorption kinetics. Wang *et al.* reported recovery times of 0.34 ns for CO and 16.84 ns for C_2H_2 on MoS_2–WS_2 heterostructures at room temperature.[67] These results demonstrate that the Au-doped silicene/MoS_2 system enables CO desorption approximately twenty times faster than the MoS_2–WS_2 heterostructure. Comparing these results with experimental benchmarks reveals the significant advantage of the proposed design. While pristine MoS_2 sensors typically exhibit poor sensitivity to non-polar gases like CO,[68] and noble-metal doped counterparts often suffer from slow recovery kinetics ranging from minutes to hours due to strong trap states,[69,70] the AuB co-doped system achieves a unique balance. It combines the high sensitivity validated in Au-functionalized experiments with a theoretically predicted ultrafast recovery (~0.1 ns), suggesting a potential breakthrough in designing reversible room-temperature sensors.

To elucidate the electronic properties of CO- and CO_2-adsorbed systems on the silicene/MoS_2 bilayer, we conduct a detailed analysis of the band structure and projected density of states (PDOS). In both the pristine silicene/MoS_2 system and the configurations with CO and CO_2 adsorption (Fig. 6a, b and **7a, b**), the band structure retains its characteristic semiconducting nature, exhibiting a well-defined band gap that coincides with a corresponding gap in the DOS near the Fermi level. Comparison with Fig. 3a reveals that the Si- and Mo-derived bands essentially preserve their relative positions within the valence and conduction regions. Upon CO and CO_2 adsorption, subtle perturbations in the band structure emerge, accompanied by weak DOS features around 3 eV (Fig. S4a and b), indicative of van der Waals interactions between the gas molecules and the surface.

The incorporation of Au dopants into the silicene/MoS_2 bilayer markedly modulates gas-surface interactions. Upon CO adsorption, Au atoms promote π back-donation into the CO π* orbitals, thereby stabilizing the adsorption complex and reducing the band gap. In contrast, CO_2, with its linear geometry and zero dipole moment, induces broader electronic dispersion, consistent with a delocalized, multi-orbital interaction mechanism.[61] Hybridization between the CO_2 π* orbitals and the d orbitals of Au and Mo in MoS_2 gives rise to hybridized bands at lower energies than those observed for CO adsorption, evidenced by a downward shift in the band structure from −1.0 to −1.2 eV (Fig. 6d).

The B-doped system (Fig. 6e, f and **7e, f**) exhibits distinct electronic features, characterized by flat bands in the band structure that correspond to sharp DOS peaks in the low-energy region. Comparison of Fig. 3c with Fig. 6e, f confirms the persistence of these flat bands after gas adsorption. Their minimal energy dispersion leads to a high density of states and enhanced electron–electron interactions. Notably, upon CO_2 adsorption, pronounced overlap between the B orbitals and the molecular orbitals of CO_2 is evident in both the band structure and PDOS. Combined with the adsorption energy values in Table 2, this observation clarifies the preferential adsorption of CO_2 over CO on the B-doped surface.

The adsorption of CO and CO_2 on the AuB co-doped silicene/MoS_2 bilayer (Fig. 6g, h and **7g, h**) induces only minor modifications in both the band structure and the overall density of states. Compared with Fig. 3d, the energy bands in Fig. 6g, h retain their relative positions and widths, with no emergence of impurity states within the band gap. This behavior indicates that the interaction between the gas molecules and the co-doped surface is primarily physisorptive, with moderate binding strength that does not trigger significant electronic reconstruction. As shown in Fig. 7g, h, the DOS near the Fermi level after adsorption displays only faint peaks associated with the CO and CO_2 π^* orbitals, suggesting limited charge transfer. The total DOS curves closely match those of the pristine substrate, confirming that the co-doped system retains its metallic character while maintaining high electrical sensitivity.

Overall, a clear contrast emerges between CO and CO_2 adsorption in their influence on the electronic structure of the modified silicene/MoS_2 systems. CO adsorption produces more pronounced perturbations near the Fermi level, reflecting localized hybridization between the CO π^* orbitals and the substrate states. These effects are particularly evident in the Au-doped system, where π back-donation from Au to CO stabilizes the adsorption complex and slightly narrows the band gap. In contrast, CO_2 adsorption induces only subtle shifts in the band structure, with the overall electronic profile remaining largely preserved across all configurations. The weak and delocalized perturbations introduced by CO_2 arise from its linear geometry and zero dipole moment, which limit direct orbital overlap and favor physisorptive interactions. Consequently, while CO adsorption gives rise to localized states and measurable electronic reconstruction, CO_2 adsorption primarily manifests as mild energy dispersion without significant modification of the substrate's semiconducting or metallic nature.

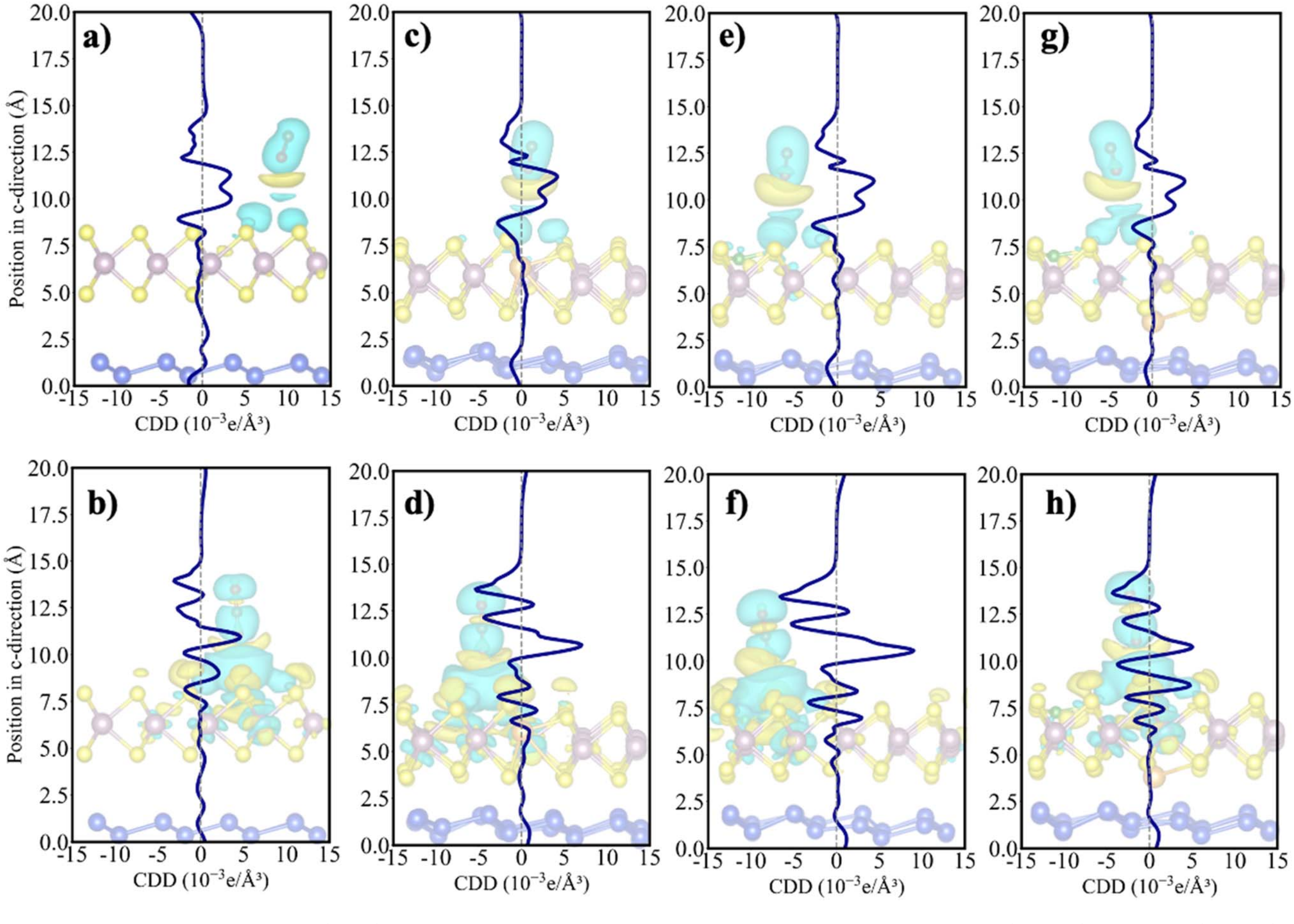

Fig. 8 The charge density difference (CDD) profiles along the *c*-direction of CO and CO_2 adsorbed on pristine (a and b), Au-doped (c and d), and B-doped (e and f), and AuB co-doped silicene/MoS_2 (g and h), respectively. The yellow iso-surface indicates areas of charge accumulation, while the cyan iso-surface represents charge depletion. These profiles are calculated by the DFT-D3 potential implemented in the VASP package.

To further elucidate the electronic interaction mechanisms at the material-gas interface, charge density difference (CDD) analyses were conducted in detail along the *c*-axis for all studied systems, as shown in Fig. 8. The resulting CDD profiles reveal pronounced charge redistribution upon CO and CO_2 adsorption on different surfaces of the silicene/MoS_2 heterostructure. For the pristine system (Fig. 8a and b), the CDD profiles indicate relatively weak interactions with both CO and CO_2, characterized by small charge accumulation regions (yellow iso-surfaces) adjacent to the gas molecules and dispersed charge depletion regions (cyan iso-surfaces) across the substrate surface. Au doping (Fig. 8c and d) induces significant changes in the CDD patterns, with substantial charge accumulation localized around the dopant site upon CO adsorption, whereas CO_2 adsorption maintains a limited interaction similar to the pristine case. Notably, B doping (Fig. 8e and f) engenders a distinct interaction mechanism, exhibiting pronounced charge depletion around the B atom for both CO and CO_2 adsorption, indicating that B acts as a strong electron acceptor and induces interfacial polarization akin to that reported for Ti-doped hBN[71] The AuB co-doped system (Fig. 8g and h) displays the most complex CDD patterns with well-organized accumulation and depletion regions for both CO and CO_2, evidencing strong activation of both gas species and consistent with enhanced adsorption properties in noble-metal-modified heterojunctions.[72] Quantitative analysis of the CDD profiles along the *c*-axis reveals an increasing charge transfer trend in the order pristine < Au-doped < B-doped < AuB co-doped, in agreement with prior studies on charge-transfer mechanisms in 2D materials for gas-sensing applications.[73] These results demonstrate that the creation of heterogeneous charge-density gradients is a key determinant of sensor sensitivity and selectivity, providing a theoretical basis for designing high-performance gas-sensing materials by modulating electronic properties through interfacial charge redistribution.[74]

Table 3 The periodic energy decomposition analyses (PEDA) of pristine and Si/MoS_2 heterostructures upon adsorption of CO and CO_2. All units are in kJ mol^{-1}. These values are calculated by the PBE potential implemented in the SCM package

Systems	PEDA types	CO	CO_2
Si/MoS_2	ΔE_{int}	−3.1	−1.5
	ΔE_{Pauli}	−0.9	4.3
	ΔE_{elstat}	−0.7	4.0
	ΔE_{orb}	−0.5	−1.8
Au-doped Si/MoS_2	ΔE_{int}	−0.4	−1.9
	ΔE_{Pauli}	−1.0	3.3
	ΔE_{elstat}	1.2	−3.3
	ΔE_{orb}	−0.6	−1.9
B-doped Sil/MoS_2	ΔE_{int}	−0.2	−1.0
	ΔE_{Pauli}	−1.1	5.3
	ΔE_{elstat}	1.5	−4.2
	ΔE_{orb}	−0.7	−2.1
AuB-doped Si/MoS_2	ΔE_{int}	−0.7	−0.4
	ΔE_{Pauli}	−1.0	4.4
	ΔE_{elstat}	0.9	−2.9
	ΔE_{orb}	−0.7	−1.9

To elucidate the nature of the adsorption interactions, periodic energy decomposition analysis (PEDA)[75] implemented in the AMS[76] is performed to calculate the intrinsic bond energies ΔE_{int} and its individual energy components. Note that

$$\Delta E_{int} = \Delta E_{eslast} + \Delta E_{Pauli} + \Delta E_{orb} \tag{3}$$

where ΔE_{elstat} is electrostatic energy, ΔE_{Pauli} stands for the Pauli repulsion energy, and ΔE_{orb} is the orbital relaxation energy of substrates + gas. Table 3 reveals the complex interaction mechanisms between the silicene/MoS_2 heterostructure and CO/CO_2 molecules. For the pristine surface, CO adsorption is primarily governed by electrostatic attraction and orbital hybridization, whereas Pauli repulsion contributes only marginally. The highly negative interaction energy ($\Delta E_{int} = -3.1$ kJ mol^{-1}), together with negative ΔE_{elstat} (−0.7 kJ mol^{-1}) and ΔE_{orb} (−0.5 kJ mol^{-1}), confirms that both charge redistribution and orbital overlap stabilize the adsorption complex. The slightly negative ΔE_{Pauli} (−0.9 kJ mol^{-1}) suggests weak electronic repulsion, consistent with a physisorption regime dominated by van der Waals interactions. In contrast, CO_2 adsorption is less favorable ($\Delta E_{int} = -1.5$ kJ mol^{-1}) due to pronounced electrostatic and Pauli repulsion, reflected by positive ΔE_{elstat} (4.0 kJ mol^{-1}) and ΔE_{Pauli} (4.3 kJ mol^{-1}). The linear, nonpolar geometry of CO_2 minimizes orbital overlap with the pristine silicene/MoS_2 surface, thereby amplifying repulsive forces. Only the modestly negative ΔE_{orb} (−1.8 kJ mol^{-1}) provides limited stabilization *via* weak π^*-surface interactions.

Au doping significantly modifies the interfacial electrostatics, reversing the sign of ΔE_{elstat} from attractive to repulsive while maintaining an overall negative ΔE_{int}. The interaction energy decreases in magnitude ($\Delta E_{int} = -0.4$ kJ mol^{-1}), and the positive ΔE_{elstat} (1.2 kJ mol^{-1}) highlights the altered surface polarization induced by Au incorporation. Nevertheless, the persistent negative ΔE_{orb} (−0.6 kJ mol^{-1}) confirms residual coupling between Au d orbitals and CO π orbitals. For CO_2 adsorption, Au doping strengthens both electrostatic ($\Delta E_{elstat} = -3.3$ kJ mol^{-1}) and orbital ($\Delta E_{orb} = -1.9$ kJ mol^{-1}) contributions, leading to a more exergonic interaction ($\Delta E_{int} = -1.9$ kJ mol^{-1}). The enhanced π^*–d orbital hybridization indicates that Au preferentially stabilizes CO_2 over CO. This conclusion is corroborated by the PDOS, which shows new hybridized states and overlapping Au d and CO_2 π^* orbitals (Fig. S4c, d and **7c**, **d**), consistent with the strongly negative ΔE_{orb} values.

B doping introduces Lewis-acidic sites that tune the balance between attractive and repulsive interactions. For CO, $\Delta E_{int} = -0.2$ kJ mol^{-1} arises from competition between electrostatic attraction ($\Delta E_{elstat} = 1.5$ kJ mol^{-1}) and Pauli repulsion ($\Delta E_{Pauli} = -1.1$ kJ mol^{-1}). In contrast, CO_2 experiences stronger binding ($\Delta E_{int} = -1.0$ kJ mol^{-1}) driven by pronounced electrostatic attraction ($\Delta E_{elstat} = -4.2$ kJ mol^{-1}) that counteracts significant Pauli repulsion ($\Delta E_{Pauli} = 5.3$ kJ mol^{-1}). The notably large negative ΔE_{orb} (−2.1 kJ mol^{-1}), the most negative across all systems, underscores the strong orbital hybridization facilitated by boron's electron-accepting character. This Lewis acidity enables efficient charge transfer from CO_2 molecular orbitals to the B p-states, forming a stable adsorption complex. The substantial overlap between B p-states and CO_2 orbitals observed in the PDOS (Fig. 6e, f and **7e, f**), along with the flat-band features in the electronic structure, directly supports the PEDA findings.

Co-doping with Au and B yields a synergistic balance between conductivity enhancement and charge localization. Au modulates the surface polarization and carrier mobility, while B provides electron-accepting sites that reinforce orbital hybridization. This cooperative effect equilibrates the Pauli and electrostatic components while maintaining a stable negative orbital term, resulting in moderate interaction energies suitable for reversible sensing. For CO, $\Delta E_{\text{int}} = -0.7$ kJ mol^{-1} with $\Delta E_{\text{Pauli}} = -1.0$ kJ mol^{-1}, $\Delta E_{\text{elstat}} = 0.9$ kJ mol^{-1}, and $\Delta E_{\text{orb}} = -0.7$ kJ mol^{-1}; for CO_2, $\Delta E_{\text{int}} = -0.4$ kJ mol^{-1} with $\Delta E_{\text{Pauli}} = 4.4$ kJ mol^{-1}, $\Delta E_{\text{elstat}} = -2.9$ kJ mol^{-1}, and $\Delta E_{\text{orb}} = -1.9$ kJ mol^{-1}. These balanced energy components ensure sufficient adsorption for detection without compromising desorption dynamics, as reflected by the minimal changes in the band structure and DOS (Fig. 6g, h and **7g, h**). The preserved metallic character and sustained orbital interactions highlight the optimized interplay of sensitivity and selectivity in the AuB co-doped silicene/MoS_2 system. In short, these analyses reveal that the adsorption processes are governed by strong electrostatic and orbital hybridization, with moderate Pauli repulsion, suggesting charge redistribution rather than covalent reconstruction at the interface. These findings align with band structure and pDOS analyses showing Au d-S p and B p-Si p hybridizations near the Fermi level, which drive the semiconductor-to-metal transition and enhance carrier mobility. The cooperative effects of Au-induced surface polarization and B-mediated electron acceptance yield balanced interaction energies, enabling substantial charge transfer without trapping. Overall, AuB co-doping efficiently tunes interfacial bonding and electronic coupling in Si/MoS_2 heterostructures, offering a rational pathway toward ultrasensitive and fast-response 2D gas sensors.

3.4. Sensitivity and selectivity analysis

To assess the practical applicability of the AuB co-doped Si/MoS_2 sensor, we systematically evaluated its cross-sensitivity toward common interfering gases, including H_2O, NH_3, and NO_2. The corresponding adsorption energies calculated using the DFT-D3 scheme are summarized in Table S4.

Notably, the sensor exhibits excellent selectivity toward ammonia, as evidenced by its extremely low adsorption energy of −12.3 meV. Such negligible interaction indicates that NH_3 induces minimal charge transfer and electronic perturbation in the sensing channel, and therefore would not generate a measurable electrical response. This behavior represents a significant advantage over many conventional metal-oxide sensors, for which NH_3 often causes severe cross-interference and signal instability.[77,78]

For humidity, H_2O exhibits a moderate adsorption energy of approximately −158.4 meV. Although this interaction is stronger than that observed for CO and CO_2, it remains within the physisorption regime. It is predominantly governed by electrostatic dipole interactions rather than the orbital-mediated charge-transfer mechanism responsible for the sensing response to carbon oxides. This finding is consistent with recent reports on the effects of humidity on two-dimensional gas sensors. It suggests that moisture interference could be effectively mitigated through standard approaches such as signal compensation or surface hydrophobic modification.[79,80]

NO_2 exhibits the strongest binding among the tested gases, with an adsorption energy of −253.8 meV, which can be attributed to its radical character and strong electrophilicity.[81] While this implies potential cross-sensitivity in NO_2-rich environments, it also reflects the high intrinsic reactivity of NO_2 commonly observed across many sensing materials. Importantly, the distinct selectivity profile of the AuB co-doped system, characterized by its insensitivity to NH_3 and its reversible detection of CO and CO_2, makes it particularly well suited for monitoring carbon oxides in agricultural and industrial environments, where ammonia is often the dominant interfering species.[82]

4. Conclusions

This study establishes the AuB co-doped Si/MoS_2 heterostructure as a highly stable and efficient platform for gas sensing. Our results demonstrate that co-doping induces a semiconductor-to-metal transition, significantly enhancing conductivity and charge transfer. Furthermore, detailed mechanistic analyses reveal a distinct selectivity for CO_2 over CO, driven by favorable orbital mixing and electrostatic attraction, while exhibiting excellent inertness toward common interfering gases such as NH_3. Crucially, the system achieves a balance between strong adsorption for detection and low energy barriers for ultrafast recovery (<0.02 ns), effectively overcoming the kinetic limitations often observed in pristine 2D sensors. These findings provide a rational pathway for designing multifunctional heterostructures with optimized sensitivity, selectivity, and reusability.

Conflicts of interest

There are no conflicts of interest to declare.

Data availability

The data supporting this article have been included as part of the supplementary information (SI). Supplementary information: possible doping sites in the Si/MoS_2 heterostructure; formation energies of Au-, B-doped, BAu-, and AuB-codoped Si/MoS_2 at different adsorption sites; adsorption energies of gases on Si/MoS_2 systems computed with different dispersion corrections; and electronic band structures and density of states of these adsorbed systems. See DOI: https://doi.org/10.1039/d5ra08262e.

Acknowledgements

This study is funded by Lac Hong University.

References

1 Y. Yang, H. Fu, F. Song, S. Yu, Z. Tang, K. Zhang, Q. Li, C. Yang, L. Zhang, J. Wang, Y. Pang, C. Wang, B. Liu, J. Chen and Q. Jing, A High-Performance H2 Gas Sensor Based on PtOx and PdOy Co-Decorating WO3 Film, *New J. Chem.*, 2025, **49**(13), 5266–5278, DOI: 10.1039/D4NJ05357E.

2 H. T. Jung, The Present and Future of Gas Sensors, *ACS Sens.*, 2022, **7**(4), 912–913, DOI: 10.1021/acssensors.2c00688.

3 B. Kwon, H. Bae, H. Lee, S. Kim, J. Hwang, H. Lim, J. H. Lee, K. Cho, J. Ye, S. Lee and W. H. Lee, Ultrasensitive N-Channel Graphene Gas Sensors by Nondestructive Molecular Doping, *ACS Nano*, 2022, **16**(2), 2176–2187, DOI: 10.1021/acsnano.1c08186.

4 K. H. Kim, M. S. Jo, S. H. Kim, B. Kim, J. Kang, J. B. Yoon and M. H. Seo, Long-Term Reliable Wireless H2 Gas Sensor via Repeatable Thermal Refreshing of Palladium Nanowire, *Nat. Commun.*, 2024, **15**(1), 1–9, DOI: 10.1038/s41467-024-53080-0.

5 J. Cao, Q. Chen, X. Wang, Q. Zhang, H.-D. Yu, X. Huang and W. Huang, Recent Development of Gas Sensing Platforms Based on 2D Atomic Crystals, *Research*, 2021, DOI: 10.34133/2021/9863038.

6 L. Ottaviano and D. Mastrippolito, The Future Ahead Gas Sensing with Two-Dimensional Materials, *Appl. Phys. Lett.*, 2023, **123**(5), 50502, DOI: 10.1063/5.0164342/2904893.

7 V. B. T. Phung, B. L. Pham, N. V. A. Duy, M. T. Dang, T. N. Tran, Q.-H. Tran, T. T. Luong and V. A. Dinh, First-Principles Study of Highly Sensitive Graphene/Hexagonal Boron Nitride Heterostructures for Application in Toxic Gas-Sensing Devices, *RSC Adv.*, 2024, **14**(7), 4904–4916, DOI: 10.1039/D3RA08017J.

8 S. U. D. Shamim, A. Siddique, B. K. Dash, T. Ahmed, S. Shaha, M. Islam and A. A. Piya, Exploring the Sensing Performance of T-Graphene, T-Boron Nitride, and Their Lateral Heterostructure for Toxic CO, NO, NO2, and SO2 Gas Molecules, *Langmuir*, 2025, **41**(13), 8726–8739, DOI: 10.1021/ACS.LANGMUIR.4C05324.

9 L. Xiao, G. Guo, M. Zhang, M. You, S. Luo, G. Guo, C. He, C. Tang and J. Zhong, Cu- and Al-Decorated Monolayer TiSe2 for Enhanced Gas Detection Sensitivity: A DFT Study, *Langmuir*, 2023, **39**(50), 18631–18643, DOI: 10.1021/ACS.LANGMUIR.3C03045.

10 S. Kumar and N. Agnihotri, Adsorption and Sensing Performance of Transition Metal Decorated Graphene Quantum Dots for AsH3, NH3, PH3, and H2S, *Langmuir*, 2024, **41**(1), 496–506, DOI: 10.1021/ACS.LANGMUIR.4C03756.

11 T. N. Tran, M. T. Dang, Q. H. Tran, T. T. Luong and V. A. Dinh, Band Valley Modification under Strain in Monolayer WSe2, *AIP Adv.*, 2022, **12**(11), 115023, DOI: 10.1063/5.0127204.

12 M. van der Laan, E. Heemskerk, F. Kienhuis, N. Diepeveen, D. Poonia, S. Kinge, M. T. Dang, V. A. Dinh, L. D. A. Siebbeles, A. Isaeva, J. van de Groep and P. Schall, Stacking-Order-Dependent Excitonic Properties Reveal Interlayer Interactions in Bulk ReS2, *ACS Photonics*, 2023, **10**(9), 3115–3123, DOI: 10.1021/ACSPHOTONICS.3C00477.

13 Q. H. Tran, T. N. Tran, T. T. Luong, V. T. Ngo, V. B. T. Phung and V. A. Dinh, Band Valley Flattening and Exciton Appearance/Disappearance under Isotropic Strain in Monolayer WS2, *Eur. Phys. J. Plus*, 2022, **137**(12), 1–11, DOI: 10.1140/EPJP/S13360-022-03537-2.

14 J. Zhang, L. Liu, Y. Yang, Q. Huang, D. Li and D. Zeng, A Review on Two-Dimensional Materials for Chemiresistive- and FET-Type Gas Sensors, *Phys. Chem. Chem. Phys.*, 2021, **23**(29), 15420–15439, DOI: 10.1039/D1CP01890F.

15 M. Donarelli and L. Ottaviano, 2D Materials for Gas Sensing Applications: A Review on Graphene Oxide, MoS2, WS2 and Phosphorene, *Sensors*, 2018, **18**(11), 3638, DOI: 10.3390/S18113638.

16 R. Peng, W. Zeng and Q. Zhou, Adsorption and Gas Sensing of Dissolved Gases in Transformer Oil onto Ru3-Modified SnS2: A DFT Study, *Appl. Surf. Sci.*, 2023, **615**, 156445, DOI: 10.1016/J.APSUSC.2023.156445.

17 A. Hunanyan, N. Petrosyan and H. Zakaryan, Gas Sensing Properties of Two Dimensional Tin Oxides: A DFT Study, *Appl. Surf. Sci.*, 2024, **672**, 160814, DOI: 10.1016/J.APSUSC.2024.160814.

18 X. Tian, S. Wang, H. Li, M. Li, T. Chen, X. Xiao and Y. Wang, Recent Advances in MoS2-Based Nanomaterial Sensors for Room-Temperature Gas Detection: A Review, *Sens. Diagn.*, 2023, **2**(2), 361–381, DOI: 10.1039/D2SD00208F.

19 S. Kim, H. Park, S. Choo, S. Baek, Y. Kwon, N. Liu, J. Y. Yang, C. W. Yang, G. Yoo and S. Kim, Active-Matrix Monolithic Gas Sensor Array Based on MoS2 Thin-Film Transistors, *Commun. Mater.*, 2020, **1**(1), 1–9, DOI: 10.1038/S43246-020-00086-Y.

20 B. Cho, M. G. Hahm, M. Choi, J. Yoon, A. R. Kim, Y. J. Lee, S. G. Park, J. D. Kwon, C. S. Kim, M. Song, Y. Jeong, K. S. Nam, S. Lee, T. J. Yoo, C. G. Kang, B. H. Lee, H. C. Ko, P. M. Ajayan and D. H. Kim, Charge-Transfer-Based Gas Sensing Using Atomic-Layer MoS2, *Sci. Rep.*, 2015, **5**(1), 1–6, DOI: 10.1038/srep08052.

21 T. E. Gber, H. Louis, A. E. Owen, B. E. Etinwa, I. Benjamin, F. C. Asogwa, M. M. Orosun and E. A. Eno, Retracted Article: Heteroatoms (Si, B, N, and P) Doped 2D Monolayer MoS2 for NH3 Gas Detection, *RSC Adv.*, 2022, **12**(40), 25992–26010, DOI: 10.1039/D2RA04028J.

22 L. Masson and G. Prévot, Epitaxial Growth and Structural Properties of Silicene and Other 2D Allotropes of Si, *Nanoscale Adv.*, 2023, **5**(6), 1574–1599, DOI: 10.1039/D2NA00808D.

23 G. Shan, H. Tan, R. Ma, H. Zhao and W. Huang, Recent Progress in Emergent Two-Dimensional Silicene, *Nanoscale*, 2023, **15**(7), 2982–2996, DOI: 10.1039/D2NR05809J.

24 B. Ouyang, S. Xiong, Z. Yang, Y. Jing and Y. Wang, MoS2 Heterostructure with Tunable Phase Stability: Strain

Induced Interlayer Covalent Bond Formation, *Nanoscale*, 2017, **9**(24), 8126–8132, DOI: 10.1039/C7NR02070H.

25 D. Lee, I. D. Kim, J. Kim, S. Kim, H. Shin, J. Lee, C. Park, Y. Ahn, H. J. Cho and S. Yuk, Three-Dimensional MoS2/MXene Heterostructure Aerogel for Chemical Gas Sensors with Superior Sensitivity and Stability, *ACS Nano*, 2023, **17**(19), 19387–19397, DOI: 10.1021/acsnano.3c07074.

26 S. Bisht, N. Dhariwal, P. Yadav, M. Chahar, D. Singh and V. Kumar, Unveiling the Impact of 2-D Materials on the Gas Sensing Properties of Metal Oxides: A Review, *J. Environ. Chem. Eng.*, 2025, **13**(2), 115980, DOI: 10.1016/J.JECE.2025.115980.

27 J. H. Shin, S. H. Jo, H. Rhyu, C. Park, M. H. Kang, W. Song, S. S. Lee, J. Lim and S. Myung, High-Performance H2S Gas Sensor Utilizing MXene/MoS2 Heterostructure Synthesized *via* the Langmuir–Blodgett Technique and Chemical Vapor Deposition, *RSC Adv.*, 2024, **14**(51), 37781–37787, DOI: 10.1039/D4RA07555B.

28 E. J. Baerends, N. F. Aguirre, N. D. Austin, J. Autschbach, F. M. Bickelhaupt, R. Bulo, C. Cappelli, A. C. T. van Duin, F. Egidi, C. Fonseca Guerra, A. Förster, M. Franchini, T. P. M. Goumans, T. Heine, M. Hellström, C. R. Jacob, L. Jensen, M. Krykunov, E. van Lenthe, A. Michalak, M. M. Mitoraj, J. Neugebauer, V. P. Nicu, P. Philipsen, H. Ramanantoanina, R. Rüger, G. Schreckenbach, M. Stener, M. Swart, J. M. Thijssen, T. Trnka, L. Visscher, A. Yakovlev and S. van Gisbergen, The Amsterdam Modeling Suite, *J. Chem. Phys.*, 2025, **162**(16), 162501, DOI: 10.1063/5.0258496/3344863.

29 M. Brandbyge, J. L. Mozos, P. Ordejón, J. Taylor and K. Stokbro, Density-Functional Method for Nonequilibrium Electron Transport, *Phys. Rev. B*, 2002, **65**(16), 165401, DOI: 10.1103/PhysRevB.65.165401.

30 C. Chen and S. P. Ong, A Universal Graph Deep Learning Interatomic Potential for the Periodic Table, *Nat. Comput. Sci.*, 2022, **2**, 718–728, DOI: 10.1038/s43588-022-00349-3.

31 E. Perim, R. Paupitz, P. A. S. Autreto and D. S. Galvao, Inorganic Graphenylene: A Porous Two-Dimensional Material with Tunable Band Gap, *J. Phys. Chem. C*, 2014, **118**(41), 23670–23674, DOI: 10.1021/jp502119y.

32 L. T. Ta, I. Hamada, Y. Morikawa and V. A. Dinh, Adsorption of Toxic Gases on Borophene: Surface Deformation Links to Chemisorptions, *RSC Adv.*, 2021, **11**(30), 18279–18287, DOI: 10.1039/D1RA02738G.

33 J. Hafner, Ab-Initio Simulations of Materials Using VASP: Density-Functional Theory and Beyond, *J. Comput. Chem.*, 2008, **29**(13), 2044–2078, DOI: 10.1002/jcc.21057.

34 H. J. Monkhorst and J. D. Pack, Special Points for Brillouin-Zone Integrations, *Phys. Rev. B*, 1976, **13**(12), 5188, DOI: 10.1103/PhysRevB.13.5188.

35 G. Kresse and D. Joubert, From Ultrasoft Pseudopotentials to the Projector Augmented-Wave Method, *Phys. Rev. B*, 1999, **59**(3), 1758, DOI: 10.1103/PhysRevB.59.1758.

36 J. P. Perdew, K. Burke and M. Ernzerhof, Generalized Gradient Approximation Made Simple, *Phys. Rev. Lett.*, 1996, **77**(18), 3865, DOI: 10.1103/PhysRevLett.77.3865.

37 S. Grimme, J. Antony and S. Ehrlich, A Consistent and Accurate Ab Initio Parametrization of Density Functional Dispersion Correction (DFT-D) for the 94 Elements H-Pu, *J. Chem. Phys.*, 2010, **132**(15), 154104.

38 S. Ehrlich, J. Moellmann and S. Grimme, Dispersion-Corrected Density Functional Theory for Aromatic Interactions in Complex Systems, *Acc. Chem. Res.*, 2012, **46**(4), 916–926, DOI: 10.1021/AR3000844.

39 T. Bučko, S. Lebègue, J. Hafner and J. G. Ángyán, Tkatchenko-Scheffler van Der Waals Correction Method with and without Self-Consistent Screening Applied to Solids, *APS*, 2013, **87**(6), 064110, DOI: 10.1103/PHYSREVB.87.064110.

40 L. Tao, E. Cinquanta, D. Chiappe, C. Grazianetti, M. Fanciulli, M. Dubey, A. Molle and D. Akinwande, Silicene Field-Effect Transistors Operating at Room Temperature, *Nat. Nanotechnol.*, 2015, **10**(3), 227–231, DOI: 10.1038/nnano.2014.325.

41 M. De Crescenzi, I. Berbezier, M. Scarselli, P. Castrucci, M. Abbarchi, A. Ronda, F. Jardali, J. Park and H. Vach, Formation of Silicene Nanosheets on Graphite, *ACS Nano*, 2016, **10**(12), 11163–11171, DOI: 10.1021/acsnano.6b06198.

42 C. Tantardini, A. G. Kvashnin, C. Gatti, B. I. Yakobson and X. Gonze, Computational Modeling of 2D Materials under High Pressure and Their Chemical Bonding: Silicene as Possible Field-Effect Transistor, *ACS Nano*, 2021, **15**(4), 6861–6871, DOI: 10.1021/acsnano.0c10609.

43 R. Yaokawa, T. Ohsuna, T. Morishita, Y. Hayasaka, M. J. S. Spencer and H. Nakano, Monolayer-to-Bilayer Transformation of Silicenes and Their Structural Analysis, *Nat. Commun.*, 2016, **7**(1), 1–6, DOI: 10.1038/ncomms10657.

44 U. Khan, M. U. Saeed, H. O. Elansary, I. M. Moussa, A. U. R. Bacha and Y. Saeed, A DFT Study of Bandgap Tuning in Chloro-Fluoro Silicene, *RSC Adv.*, 2024, **14**(7), 4844–4852, DOI: 10.1039/D3RA07452H.

45 R. Zhang, Y. Hou, X. Guo, X. Chen, W. Li, X. Tao and Y. Huang, Elucidating the Effects of B/Al Doping on the Structure Stability and Electrochemical Properties of Silicene Using DFT, *Phys. Chem. Chem. Phys.*, 2023, **25**(38), 26353–26359, DOI: 10.1039/D3CP03116K.

46 R. Pawlak, C. Drechsel, P. D'Astolfo, M. Kisiel, E. Meyer and J. I. Cerda, Quantitative Determination of Atomic Buckling of Silicene by Atomic Force Microscopy, *Proc. Natl. Acad. Sci. U. S. A.*, 2020, **117**(1), 228–237, DOI: 10.1073/PNAS.1913489117.

47 D. da S. Gomes, L. A. Ribeiro and M. L. Pereira, Predicting Irida-Silicene: A Novel 2D Silicon Allotrope, *ACS Omega*, 2024, **9**(51), 50570–50578, DOI: 10.1021/acsomega.4c08395.

48 B. Gao, Y. Zhao, X. Du, D. Qian, S. Ding, C. Xiao, J. Wang, Z. Song and H. W. Jang, Modulating Trinary-Heterostructure of MoS2 via Controllably Carbon Doping for Enhanced Electrocatalytic Hydrogen Evolution Reaction, *Adv. Funct. Mater.*, 2023, **33**(22), 2214085, DOI: 10.1002/adfm.202214085.

49 X. Wang, G. Zhao, X. Lv, M. Zhao, W. Wei and G. Liu, Effect of Doping and Defects on the Electronic Properties of MoS2/WSe2 Bilayer Heterostructure: A First-Principles Study, *Phys.*

Chem. Chem. Phys., 2024, **26**(26), 18402–18407, DOI: 10.1039/D4CP01673D.

50 H. Lim, S. Yu, W. Choi and S. O. Kim, Hierarchically Designed Nitrogen-Doped MoS2/Silicon Oxycarbide Nanoscale Heterostructure as High-Performance Sodium-Ion Battery Anode, *ACS Nano*, 2021, **15**(4), 7409–7420, DOI: 10.1021/acsnano.1c00797.

51 S. R. Tavares, V. S. Vaiss, F. P. N. Antunes, C. G. Fonseca, I. M. Nangoi, P. I. R. Moraes, C. V. Soares, J. F. S. Haddad, L. L. Lima, B. N. N. Silva and A. A. Leitão, DFT Calculations for Structural Prediction and Applications of Intercalated Lamellar Compounds, *Dalton Trans.*, 2018, **47**(9), 2852–2866, DOI: 10.1039/C7DT03730A.

52 H. Van Ngoc, Study of Antimony-Doped Silicene Nanoribbons in the Electric Field, *Macromol. Symp.*, 2023, **410**(1), 2100279, DOI: 10.1002/MASY.202100279.

53 D. da S. Gomes, L. A. Ribeiro and M. L. Pereira, Predicting Irida-Silicene: A Novel 2D Silicon Allotrope, *ACS Omega*, 2024, **9**(51), 50570–50578, DOI: 10.1021/acsomega.4c08395.

54 K. R. Abidi and P. Koskinen, Electronic Structure and Elasticity of Two-Dimensional Metals of Group 10: A DFT Study, *J. Phys.: Conf. Ser.*, 2023, **2518**(1), 012006, DOI: 10.1088/1742-6596/2518/1/012006.

55 M. Baithi, D. L. Duong, M. Baithi and D. L. Duong, Doped, Two-Dimensional, Semiconducting Transition Metal Dichalcogenides in Low-Concentration Regime, *Crystals*, 2024, **14**(10), 832, DOI: 10.3390/CRYST14100832.

56 X. Li, J. T. Mullen, Z. Jin, K. M. Borysenko, M. Buongiorno Nardelli and K. W. Kim, Intrinsic Electrical Transport Properties of Monolayer Silicene and MoS2 from First Principles, *Phys. Rev. B: Condens. Matter Mater. Phys.*, 2013, **87**(11), 115418, DOI: 10.1103/PhysRevB.87.115418.

57 A. M. Barboza, L. C. R. Aliaga, D. F. de Faria and I. N. Bastos, Unveiling the structure and interactions of silicene grown on MoS2: insights from hybrid molecular dynamics simulations, *Acta Crystallogr., Sect. B:Struct. Sci., Cryst. Eng. Mater.*, 2025, **81**, 533–539, DOI: 10.1107/S2052520625009187.

58 N. Gao, J. C. Li and Q. Jiang, Tunable Band Gaps in Silicene–MoS2 Heterobilayers, *Phys. Chem. Chem. Phys.*, 2014, **16**(23), 11673–11678, DOI: 10.1039/C4CP00089G.

59 S. Y. Cho, S. J. Kim, Y. Lee, J. S. Kim, W. B. Jung, H. W. Yoo, J. Kim and H. T. Jung, Highly Enhanced Gas Adsorption Properties in Vertically Aligned MoS2 Layers, *ACS Nano*, 2015, **9**(9), 9314–9321, DOI: 10.1021/acsnano.5b04504.

60 M. A. Ramzan, R. Favre, S. N. Steinmann, T. Le Bahers and P. Raybaud, Electrocatalytic Reduction Mechanisms of CO2 on MoS2 Edges Using Grand-Canonical DFT: From CO2 Adsorption to HCOOH or CO, *J. Phys. Chem. C*, 2024, **128**(24), 10025–10034, DOI: 10.1021/acs.jpcc.4c03266.

61 F. M. Enujekwu, C. I. Ezeh, M. W. George, M. Xu, H. Do, Y. Zhang, H. Zhao and T. Wu, A Comparative Study of Mechanisms of the Adsorption of CO2 Confined within Graphene–MoS2 Nanosheets: A DFT Trend Study, *Nanoscale Adv.*, 2019, **1**(4), 1442–1451, DOI: 10.1039/C8NA00314A.

62 D. K. Nguyen, D. Q. Hoang and D. M. Hoat, Exploring a Silicene Monolayer as a Promising Sensor Platform to Detect and Capture NO and CO Gas, *RSC Adv.*, 2022, **12**(16), 9828–9835, DOI: 10.1039/D2RA00442A.

63 T. Pham, G. Li, E. Bekyarova, M. E. Itkis and A. Mulchandani, MoS 2 -Based Optoelectronic Gas Sensor with Sub-Parts-per-Billion Limit of NO 2 Gas Detection, *ACS Nano*, 2019, **13**(3), 3196–3205, DOI: 10.1021/acsnano.8b08778.

64 L. Qi, Y. Wang, L. Shen and Y. Wu, Chemisorption-Induced n -Doping of MoS2 by Oxygen, *Appl. Phys. Lett.*, 2016, **108**(6), 063103, DOI: 10.1063/1.4941551/594150.

65 F. Schedin, A. K. Geim, S. V. Morozov, E. W. Hill, P. Blake, M. I. Katsnelson and K. S. Novoselov, Detection of Individual Gas Molecules Adsorbed on Graphene, *Nat. Mater.*, 2007, **6**(9), 652–655, DOI: 10.1038/nmat1967.

66 R. Rahimi, M. Solimannejad and A. Horri, DFT Study of the Adsorption Properties and Sensitivity of a B2N Monolayer toward Harmful Gases, *Sci. Rep.*, 2024, **14**(1), 29282, DOI: 10.1038/s41598-024-77659-1.

67 T. Tian, X. Zhou, J. Yu, J. Bai, L. Chen, N. He, X. Li, H. Zhang and H. Cui, First-Principles Predictions of MoS2-WS2 In-Plane Heterostructures for Sensing Dissolved Gas Species in Oil-Immersed Transformers, *ACS Omega*, 2024, **9**(18), 20253–20262, DOI: 10.1021/acsomega.4c00681.

68 D. Burman, H. Raha, B. Manna, P. Pramanik and P. K. Guha, Substitutional Doping of MoS2 for Superior Gas-Sensing Applications: A Proof of Concept, *ACS Sens.*, 2021, **6**(9), 3398–3408, DOI: 10.1021/ACSSENSORS.1C01258.

69 L. Zhao, X. Wang, Z. Zhang, Y. Ji, J. Guo, Z. Du and G. Cheng, Realizing the Ultrafast Recovery of the Monolayer MoS2-Based NH3 Sensor by Gas-Ion-Gate, *ACS Appl. Mater. Interfaces*, 2025, **17**(11), 17465–17475, DOI: 10.1021/ACSAMI.4C19870.

70 D. J. Late, B. Liu, H. S. S. R. Matte, V. P. Dravid and C. N. R. Rao, Hysteresis in Single-Layer MoS2 Field Effect Transistors, *ACS Nano*, 2012, **6**(6), 5635–5641, DOI: 10.1021/NN301572C.

71 B. A. Kalwar, W. Fangzong, A. M. Soomro, M. R. Naich, M. H. Saeed and I. Ahmed, Highly Sensitive Work Function Type Room Temperature Gas Sensor Based on Ti Doped HBN Monolayer for Sensing CO2, CO, H2S, HF and NO. A DFT Study, *RSC Adv.*, 2022, **12**(53), 34185–34199, DOI: 10.1039/D2RA06307G.

72 K. Gao, H. Chen, J. Ding, M. Yang, H. Fu and J. Peng, Enhanced Adsorption Properties of Noble Metal Modified MoS2/WS2 Heterojunctions, *Adv. Theory Simul.*, 2025, **8**(3), 2400949, DOI: 10.1002/ADTS.202400949.

73 T. Kim, T. H. Lee, S. Y. Park, T. H. Eom, I. Cho, Y. Kim, C. Kim, S. A. Lee, M. J. Choi, J. M. Suh, I. S. Hwang, D. Lee, I. Park and H. W. Jang, Drastic Gas Sensing Selectivity in 2-Dimensional MoS2 Nanoflakes by Noble Metal Decoration, *ACS Nano*, 2023, **17**(5), 4404–4413, DOI: 10.1021/acsnano.2c09733.

74 K. Weng, J. Peng, Z. Shi, A. Arramel and N. Li, Highly NH3 Sensitive and Selective Ti3C2O2-Based Gas Sensors: A Density Functional Theory-NEGF Study, *ACS Omega*, 2023, **8**(4), 4261–4269, DOI: 10.1021/acsomega.2c07492.

75 M. Raupach and R. Tonner, A Periodic Energy Decomposition Analysis Method for the Investigation of Chemical Bonding in Extended Systems, *J. Chem. Phys.*, 2015, **142**(19), 194105, DOI: 10.1063/1.4919943/194148.

76 C. J. O. Verzijl and J. M. Thijssen, DFT-Based Molecular Transport Implementation in ADF/BAND, *J. Phys. Chem. C*, 2012, **116**(46), 24393–24412, DOI: 10.1021/jp3044225.

77 Z. Cui, H. Wang, K. Yang, Y. Shen, K. Qin, P. Yuan and E. Li, Highly Sensitive and Selective Defect WS2 Chemical Sensor for Detecting HCHO Toxic Gases, *Sensors*, 2024, **24**(3), 762, DOI: 10.3390/s24030762.

78 Z. Cui, H. Wu, K. Yang, X. Wang and Y. Lv, Adsorption of Gas Molecules on Intrinsic and Defective MoSi2N4 Monolayer: Gas Sensing and Functionalization, *Sens. Actuators, A*, 2024, **366**, 114954, DOI: 10.1016/j.sna.2023.114954.

79 Y. Shen, P. Yuan, Z. Yuan, Z. Cui, D. Ma, F. Cheng, K. Qin, H. Wang and E. Li, The O-Defective g-ZnO Sensor for VOC Gases: The Adsorption-Desorption, Electronic, and Sensitivity Properties, *Langmuir*, 2024, **40**(33), 17396–17404, DOI: 10.1021/acs.langmuir.4c01491.

80 M. Guo, T. Zhao and Z. Cui, Adsorption Behavior and Sensing Performance of VOCs on Monolayer XC (X=Ge, Si), *Surf. Interfaces*, 2024, **51**, 104607, DOI: 10.1016/j.surfin.2024.104607.

81 Z. Cui, K. Yang, Y. Shen, Z. Yuan, Y. Dong, P. Yuan and E. Li, Toxic Gas Molecules Adsorbed on Intrinsic and Defective WS2: Gas Sensing and Detection, *Appl. Surf. Sci.*, 2023, **613**, 155978, DOI: 10.1016/j.apsusc.2022.155978.

82 Z. Cui, X. Wang, Y. Ding, E. Li, K. Bai, J. Zheng and T. Liu, Adsorption of CO, NH3, NO, and NO2 on Pristine and Defective g-GaN: Improved Gas Sensing and Functionalization, *Appl. Surf. Sci.*, 2020, **530**, 147275, DOI: 10.1016/j.apsusc.2020.147275.